ISTFA 2023: Proceedings of the 49th International
Symposium for Testing and Failure Analysis Conference
November 12—16, 2023, Phoenix, Arizona, USA
https://doi.org/10.31339/asm.cp.istfa2023p0092



# A Multiscale and Multimodal Correlative Microscopy Workflow to Characterize Copper Segregations Identified in Epitaxial Layer of Power MOSFETs

***Flavio Cognigni and Marco Rossi***
*Dept. of Basic and Applied Sciences for Engineering (SBAI)*
*Research Center on Nanotechnologies Applied to Engineering of Sapienza (CNIS)*
*Sapienza University of Rome*
*flavio.cognigni@uniroma1.it*

***Heiko Stegmann***
*Carl Zeiss Microscopy GmbH, Oberkochen, Germany*
*heiko.stegmann@zeiss.com*

***Giuseppe Sciuto, Giuseppe Anastasi, Massimiliano Astuto, Marco Bonadonna, Domenico Mello***
*STMicroelectronics, Strada Primosole 50, Catania, Italy*
*domenico.mello@st.com*

## Abstract

Power MOSFETs are electronic devices that are commonly used as switches or amplifiers in power electronics applications such as motor control, audio amplifiers, power supplies and illumination systems. During the fabrication process, impurities such as copper can become incorporated into the device structure, giving rise to defects in crystal lattice and creating localized areas of high resistance or conductivity. In this work we present a multiscale and multimodal correlative microscopy workflow for the characterization of copper inclusions found in the epitaxial layer in power MOSFETs combining Light Microscopy (LM), non-destructive 3D X-ray Microscopy (XRM), Focused-Ion Beam Scanning Electron Microscopy (FIB-SEM) tomography coupled with Energy Dispersive X-ray Spectroscopy (EDX), and Transmission Electron Microscopy (TEM) coupled with Electron Energy Loss Spectroscopy (EELS). Thanks to this approach of correlating 2D and 3D morphological insights with chemical information, a comprehensive and multiscale understanding of copper segregations distribution and effects at the structural level of the power MOSFETs can be achieved.

## Introduction

Conventional high-voltage planar MOSFETs are limited, since the blocking or drain-to-source breakdown voltages depend on thickness, doping, and geometry. Superjunction MOSFETs overcome these limitations with deep, narrow trenches etched into the wafer. MDmesh power MOSFETs are ideal for Switched-Mode Power Supplies in applications ranging from data center servers and 5G infrastructure to flat panel televisions [1, 2]. This technology, developed by STMicroelectronics, is based on silicon, multi-drain, Superjunction, and N-channel, achieving its RDS(ON) per area performance by improving the transistor drain structure to lower the drain-source voltage drop [3]. The Superjunction Multi-drain structure consists of a sequence of epitaxial growths and drains designed to maintain the required voltage class for the product. However, in some cases, contaminants, or defects in the bulk formation of the device can lead to failures in high leakage (IDSS) or soft breakdown voltage (BVDSS). Consequently, the quality of the epitaxial layers plays a crucial role in preventing such issues.

Therefore, the development of a multiscale and multimodal correlative microscopy (CM) workflow is of paramount importance to get a comprehensive defect localization and analysis, as well as in understanding and addressing the issues related to the epitaxial layers in Superjunction Multi-drain MOSFETs. CM refers to the process of integrating different investigation modalities to provide a holistic understanding of the sample's structural and functional properties [4, 5, 6]. The implementation of correlative microscopy workflows requires the support of sophisticated hardware and software solutions that allow researchers to localize the Regions of Interest (ROIs) within the sample and subsequently investigate the same ROIs combining a set of characterization tools to provide information about the morphology, topology, and chemistry of the specimen across multiple length scales [6, 7, 8, 9].

In this work, we present an innovative multiscale and multimodal CM workflow to detect and characterize impurities in the epitaxial layers of Superjunction MOSFETs (Fig. 1). However, the same principles and guidelines can be adopted in further workflows in the field of electronics and semiconductor failure analysis and research.

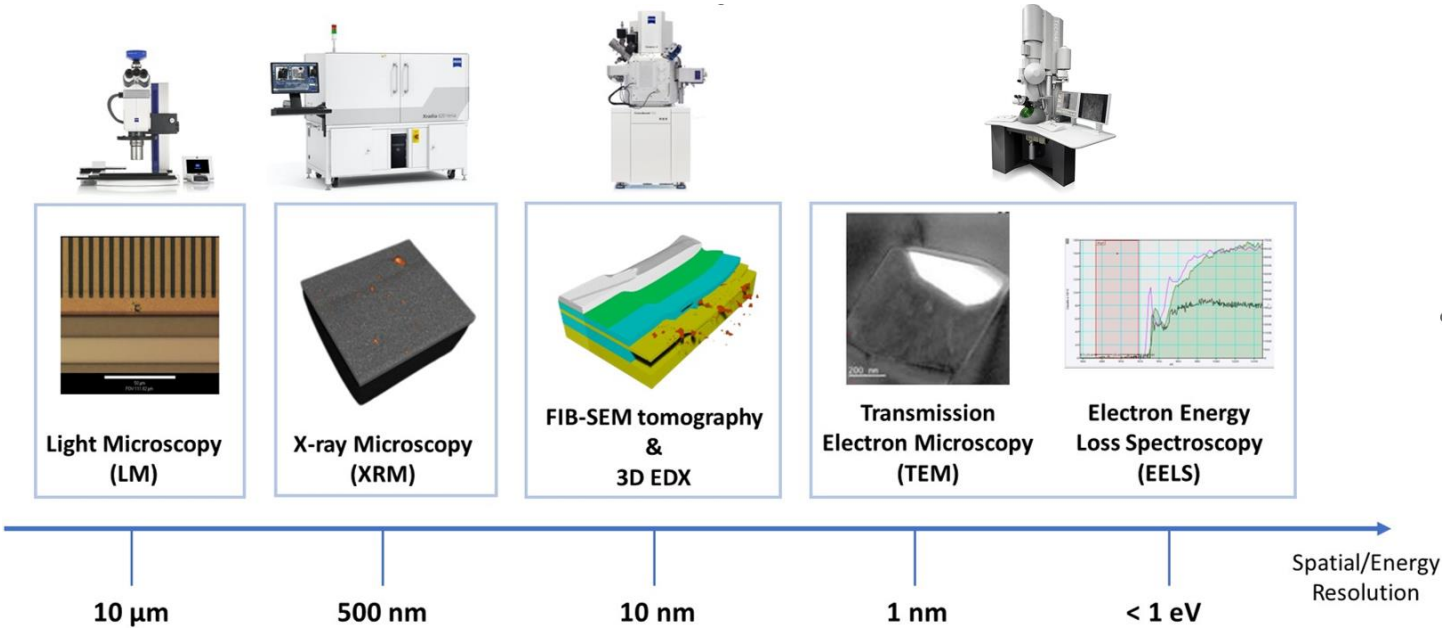


***Fig. 1*** *– The multiscale and multimodal correlative microscopy workflow used in this work involved several characterization techniques to reach a comprehensive understanding of the defects providing information of the morphology, topology, and chemistry across the length scales reported in the figure.*

The samples under analysis were halted during the parametric test due to an unexpected trend in the measurement of soft breakdown voltage (BVDSS). The CM workflow was then employed involving Light Microscopy (LM) observations of the in-line defects detected after epitaxy, with subsequent characterization using X-Ray Microscopy (XRM) and Focused-Ion Beam Scanning Electron Microscopy (FIB-SEM) tomography, supported by 3D Energy Dispersive X-ray Spectroscopy (EDX) and Transmission Electron Microscopy (TEM) coupled with Electron Energy Loss Spectroscopy (EELS).

LM is an essential tool for observing samples at relatively low magnifications. Its importance lies in providing a quick and non-destructive initial overview of the material's surface. It allows researchers to identify in-line defects after epitaxy, which serves as a starting point for further investigation [10].

XRM allows researchers to study the internal structure of materials non-destructively and is particularly useful for characterizing materials with high density contrast, providing 3D information about defects, porosity, and grain structures. XRM has been involved in a wide range of applications such as energy materials research [11, 12, 13, 14], electronics and semiconductors [15, 16, 17], aerospace [18, 19], impact behavior characterization [20, 21], cultural heritage [22, 23, 24, 25], biomedical engineering [26, 27], and life sciences [28, 29].

FIB-SEM tomography, coupled with 3D EDX, combines focused-ion beam milling, scanning electron microscopy and chemical element mapping. It permits imaging of the sample's internal structure at very high resolution, making it an excellent technique for characterizing nanoscale features and their elemental composition [30, 31].

TEM provides sub-nanoscale resolution images and is particularly useful for studying the atomic and nanoscale structure of materials [32]. This technique can be coupled with EELS, providing information about the elemental composition and electronic properties of the material at the atomic scale [33].

## Materials and Methods

*Light Microscopy (LM)*

LM investigations were performed using ZEISS Axio Zoom V.16 and ZEISS ZEN Core 3.5 software [34]. The CM environment was provided by Zeiss ZEN Connect software [35].

*CAD Navigation*

Dies were identified and navigated using the Avalon Synopsys wafer map software [36].

*X-ray Microscopy (XRM)*

X-ray Microscopy (XRM) experiments were performed using a Zeiss Xradia Versa 620. XRM scans were performed setting a source voltage and power of 160 kV and 25 W using an LE2 source filter. We selected the 4x objective to reach a pixel size of 1.0 µm and acquire 2401 projections.

*Focused-Ion Beam Scanning Electron Microscopy (FIB-SEM) tomography*

The FIB-SEM 3D data acquisition was carried out using a ZEISS Crossbeam 350 FIB-SEM instrument, and the Atlas 3D software module [37]. A 14 x 20 x 1 $\mu m^3$ platinum layer was ion beam deposited on top of the target area. A set of diagonal

and straight lines was FIB cut into the platinum layer, and then covered by an ion beam deposited carbon layer of 14 x 20 x 1 $\mu m^3$ size. A large trench was FIB milled in front of the volume of interest to make it accessible for the subsequent repeated slice milling with the FIB and imaging with the SEM. Slight slice thickness variations and lateral drifts during data acquisition are unavoidable and would eventually lead to distortions of the sample structures in the 3D visualization. Therefore, the mentioned lines serve as fiducials for measurement and dynamic correction of slice thickness during data acquisition, as well as for correction of lateral drift and for periodic electron beam tuning [3]. For slicing the Volume of Interest (VOI), a FIB probe of 30 kV and 700 pA was used. The SEM probe used for imaging was 2 kV and 1 nA. A pixel size of 10 nm and a slice thickness target of 20 nm was used for the imaging data acquisition.

*3D Energy Dispersive X-ray Spectroscopy (EDX)*
The Atlas 3D system allows to record EDX maps at fixed intervals, in addition to the SEM images of the advancing cross-section. Here, an EDX map was acquired after every 50th imaging slice, thus every 1000 nm, using an SEM probe of 16 kV, 2 nA and a pixel size of 25 nm. Initial top-down EDX maps of the defect area were obtained in the same instrument at the same SEM settings. The EDX detector used was an Oxford Instruments Ultim Max 100.

*Image Reconstruction and Processing*
XRM datasets were reconstructed using the Scout-and-Scan Control System Reconstructor (V.16.1.14271.44713) [38] employing the Feldkamp-Davis-Kress (FDK) reconstruction algorithm [39]. Residual image shifts and slice thickness variations of the FIB-SEM tomography dataset acquired were corrected using the Atlas 3D software module. The defects localization process was performed using ZEISS ZEN Connect module of the ZEISS ZEN Core 3.5 software. Dragonfly Pro software (Version 2022.1 Build 1259) from Object Research Systems (ORS) [40] was used to visualize, mutually align, analyze, and process the different datasets. Datasets were processed using a Non-local Means (Kernel Size: 7, Smoothing 0.5) filter to reduce noise while preserving sharp edges.

*Transmission Electron Microscopy (TEM)*
High magnification analyses were performed using a TEM Thermo Fisher Scientific Tecnai F20 equipped with Gatan Imaging Filter (GIF) Continuum for EELS analyses and Oxford Instruments Xplore 80$mm^2$ EDX detector. The samples were prepared by ZEISS Crossbeam 550L FIB-SEM system equipped with micromanipulator Oxford Instruments Omniprobe 400. This equipment was used to follow the standard approach for lamella preparation [41] with in situ lift-out extraction. The localization of the point of analysis was performed by ZEISS ZEN Connect software.

## Results and Discussion

As mentioned earlier, wafers were considered that exhibited a soft trend in breakdown voltage measurement. Fault Isolation did not show any significant hot spots, so we expanded our investigation of the defects found to all the steps of the flow. In particular, we focused our attention on some promising classes of defects that seemed to have the same topology as the electrical map.. The main problem is that the wafer is not in the same process step as the inspection. In fact, the inspection tool indicates the position of the defects with respect to a point in the center of the wafer which it finds in a rather coarse way (with an indetermination which can also be of the order of hundreds of μm). In the analysis phase, the defect is identified by moving in the area in which it is located thanks to appropriate software and then on sight by exploiting the structures visible in the surrounding areas. In the absence of visible areas as in this case because they are now buried by the overlying layers, a precise location is rather difficult. In this case we used Synopsys CAD Navigator Avalon and thanks to the wafer map we identified the position of the die in the wafer (Fig. 2a). Then, based on the photos taken during the inspection phase, we calculate the x and y offsets of the inspection reference center with respect to the real wafer center point. This way we are able to place defects on layouts for precise localization. However, this very effective technique in digital devices is often impossible to apply in power devices. In fact, due to the size of the structures it is not possible to extrapolate the data necessary for the calculation of the offsets from the images.

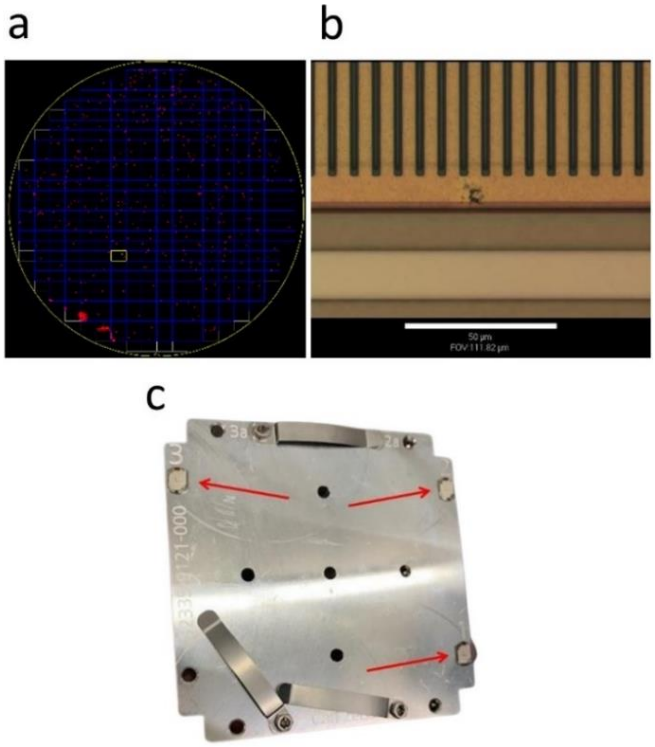


***Fig. 2*** *– Defect localization by CAD nav. (a) Defect position on the wafer and (b) on the device. (c) The CM sample holder features three fiducial markers to define a reference coordinate system, easing the application of the CM workflow.*

As happened in this specific case where there was not enough information for a precise localization of the defect (and, in any

case, not enough to properly address an XRM or FIB-SEM tomography analysis). Therefore, the defects were located and imaged using LM addressed from CAD info (Fig. 2b) and transferred on XRM and FIB using CM. The CM approach makes use of a dedicated sample holder that features fiducial markers (Fig. 2c) to define a reference coordinate system to facilitate the application of the CM workflow.

LM is a valuable technique for observing samples at relatively low magnification providing a quick and non-destructive initial overview of the material's surface [10]. The defect location area was first imaged and reconstructed using LM imaging (Fig. 3a). This investigation was performed to determine if the defect area generated a concave or convex altered geometry. The defects localization protocol used with ZEISS ZEN Connect allowed to easily navigate the specimen and relocate specific ROIs when moving from one characterization platform to the other. An SEM micrograph of the same defect observed using LM is reported in Fig. 3b.

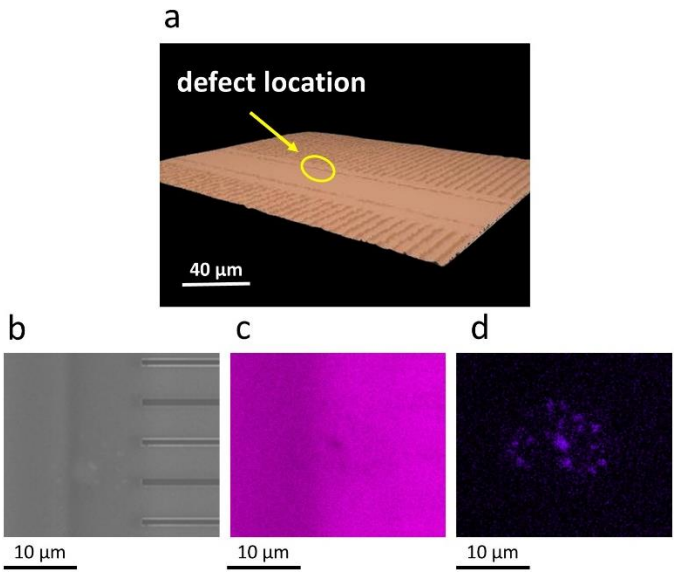


***Fig. 3*** *– (a) LM image of the device where the defect location is highlighted by the yellow circle. The defect location coordinates were transferred to the SEM to obtain (b) a micrograph of the defect and (c) Si-K and (d) Cu-K elemental maps.*

Initial top-down EDX elemental mapping of the defect showed Copper (Cu)-rich spots that coincide with slightly Silicon (Si)-depleted areas (Fig. 3c-d), while the maps for other elements showed no irregularities. However, such simple top-down maps do not provide information about the exact depth and shape of the Cu-rich spots.

Therefore, XRM experiments were performed since it allows for 2D/3D non-destructive investigation with a multiscale approach, unlocking information about the internal microstructure and phase composition of an object by exploiting the radiation-matter interaction [12, 42]. A Volume of Interest (VOI) of 0.83 $mm^3$ was investigated. Some copper (Cu) inclusions in the epitaxial layer show higher X-ray attenuation compared to the silicon (Si) substrate, so in the 2D slice of Fig. 4a, they are depicted as shining spots. Thanks to the XRM's ability to provide three-dimensional data, we had the chance to highlight that Cu segregations of different shapes and sizes are distributed all over the area between the epitaxial layer and gate, as shown in Fig. 4b. Indeed, using a histogram-based thresholding method, we were able to segment the Cu segregations scattered in the XRM volume, shown in orange in Fig. 4b. The XRM investigation revealed crucial insights related to the distribution of Cu segregations: while the initial LM images suggested that samples were characterized by a single defect site, extending the analysis to the third dimension by investigating the full volume of interest (VOI) revealed that Cu inclusions are scattered over the area of the epitaxial layer and below the gate oxide.

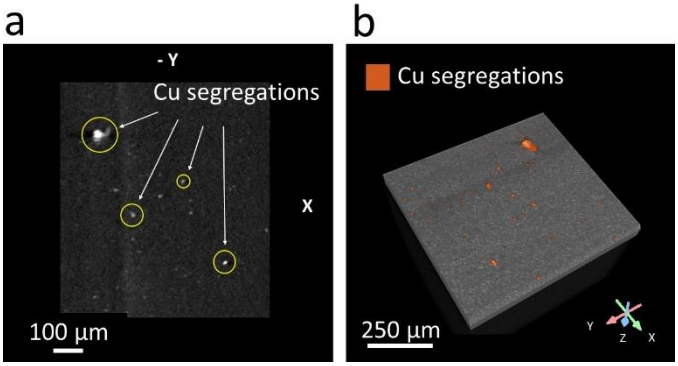


***Fig. 4*** *– XRM investigation provided (a) 2D slices and (b) 3D datasets. A histogram-based thresholding method allowed the segmentation of Cu inclusions. That are depicted as shining spots.*

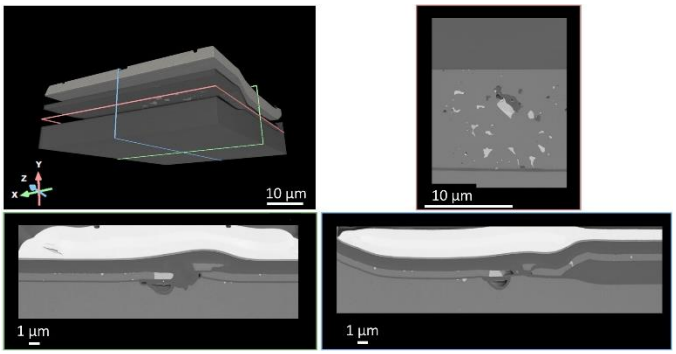


***Fig. 5*** *– Volume rendering and 2D slices in the XZ, XY and YZ planes extracted from the FIB-SEM tomography dataset.*

After localizing the defect, it was also targeted for FIB-SEM tomography coupled with 3D EDX by correlating structures on the sample surface that are visible in FIB imaging with the same structures shown in the LM image.

The reconstructed FIB-SEM tomography dataset is shown in Fig. 5, along with three cross-sections in the XZ, XY, and YZ planes. These images confirm the initial observations made

using XRM: Cu segregations are scattered over the investigation volume and exhibit different shapes and dimensions. In addition, this protocol opened the possibility of computing statistical properties related to the Mean Feret Diameter (MFD) of Cu inclusions: To obtain more information about the dimensions of the Cu segregations, we performed a histogram-based thresholding on the FIB-SEM tomography dataset to segment the features of interest, i.e., the Cu segregations (Fig. 6a). After the segmentation we measured the MFD of the Cu segregations. The Feret diameter is measured by selecting two points on opposite sides of the object's boundary that are farthest apart and measuring the distance between them along various directions. The mean Feret diameter is then calculated as the average of all these measurements. This parameter is particularly suitable for applications such as particle/segregation dimensional analysis [43].

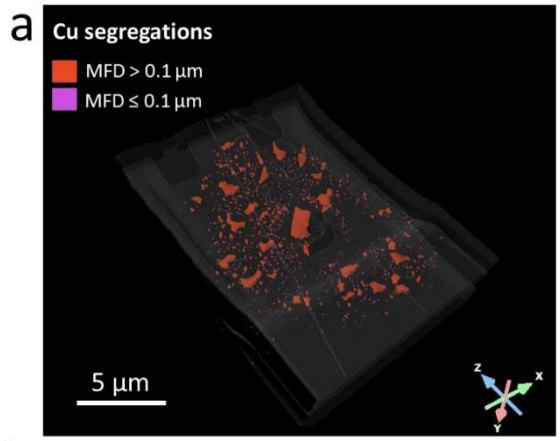


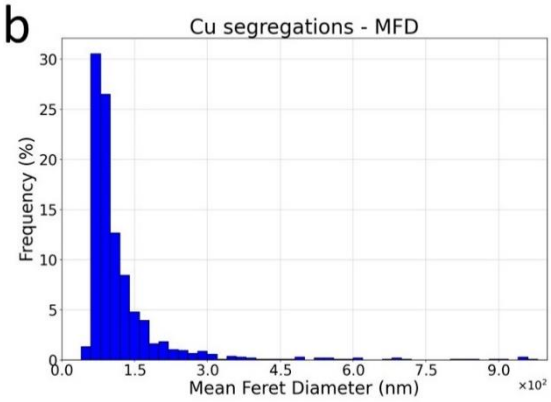


| Statistic | Mean Feret Diameter (µm) |
|---|---|
| Mean | 130.50 |
| Max | 1,962.61 |
| Min | 57.59 |
| Standard Deviation | 140.95 |

***Fig. 6*** *– The Mean Feret Diameter (MFD) of Cu segregations was investigated. (a) Cu segregations were segmented via a histogram-based thresholding method revealing that 62.7% of Cu segregations shown a 57.60 nm ≤ MFD ≤ 104.60 nm (purple) whilst the remaining 37.3% was characterized by a 104.6 nm < MFD ≤ 1.96·10$^3$ nm (orange).*

The histogram and the statistical properties related to the MFD investigation are reported in Fig. 6b. These results allowed us to notice that Cu segregations can be split into two different populations according to their MFD values. Specifically, 62.7% (653 out of 1041 particles) of Cu segregations showed a 57.60 nm ≤ MFD ≤ 104.60 nm (purple, Fig. 6a), while the remaining 37.3% (388 particles) were characterized by a 104.6 nm < MFD ≤ 1.96·10$^3$ nm (orange, Fig. 6a). The overall mean MFD was 130.5 µm.

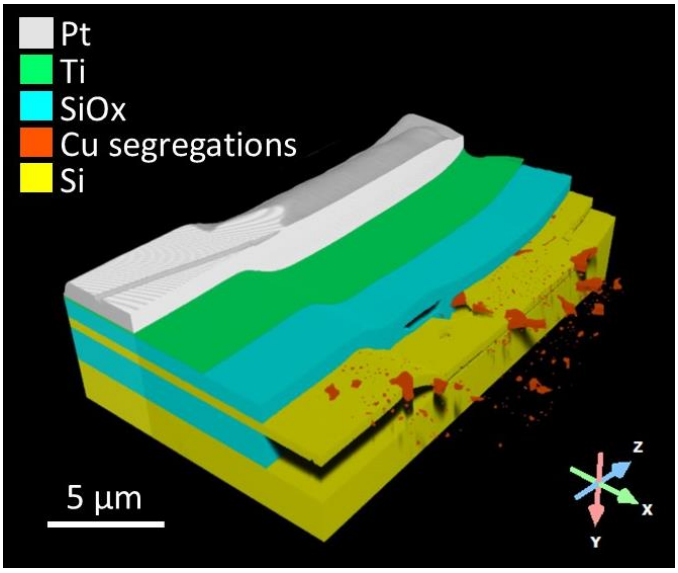


***Fig. 7*** *– The EDX maps acquired during the FIB-SEM tomography experiment were used as a driving tool for further segmentation and 3D rendering.*

As mentioned previously, EDX maps were also acquired at fixed intervals during the FIB-SEM tomography data acquisition, in addition to the SEM images of the advancing cross-section The elemental maps were used to drive further segmentation of the FIB-SEM tomography dataset. This experiment allowed us to create a color-coded three-dimensional rendering (Fig. 7) where the Platinum (Pt) layer, used to support the FIB-SEM tomography experiment, is shown in white, along with Titanium (Ti, green), Silicon oxide (SiOx, light blue), Cu segregations (orange), and Si layer (yellow). This 3D chemical map provided valuable morphological and compositional information about the defect location, as previously obtained via XRM, but with higher resolution. Coupling FIB-SEM with 3D EDX maps enabled a comprehensive understanding and characterization of the defect area, including chemical/elemental information.

Based on correlative coordinates, a lamella was prepared from another similar defect to observe the specimen at higher magnification using TEM. In Fig. 8a, we present the TEM morphological overview of the defect area. Several enlarged views of specific ROIs are displayed in Fig. 8b-c-d. These images confirm the presence of a large population of small-scale Cu segregations around the larger one. These results are

consistent with the previous observations performed using FIB-SEM tomography.

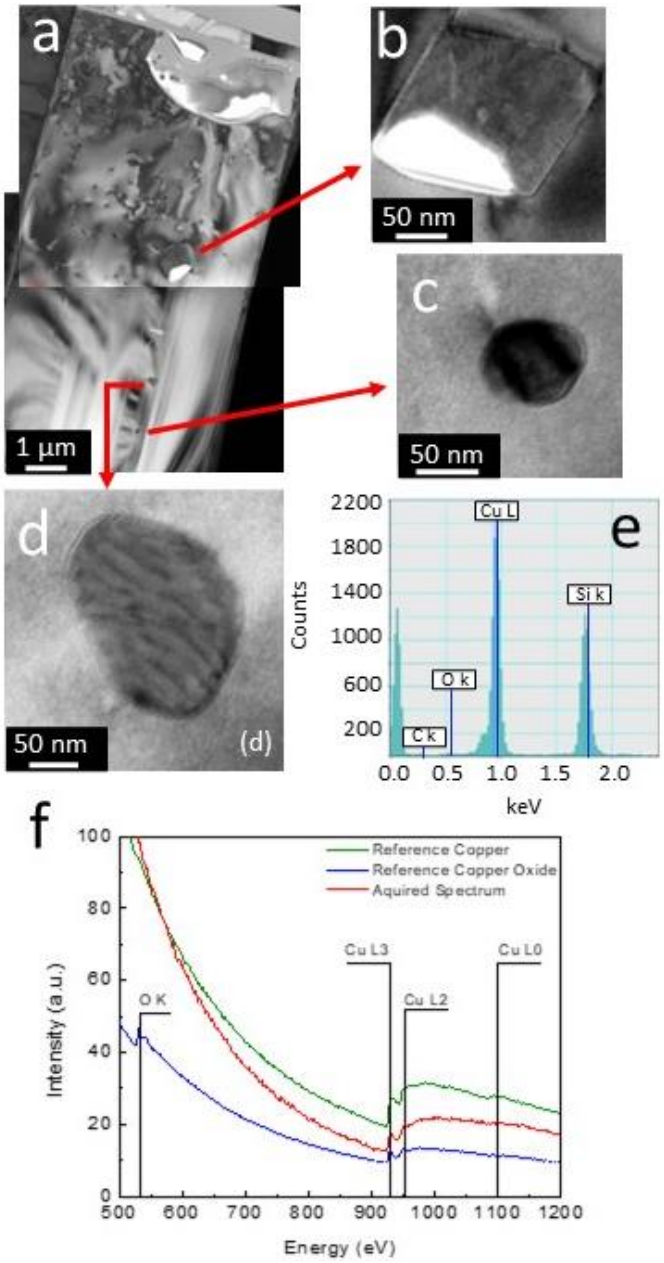


***Fig. 8*** *– (a) TEM morphological overview with (b-c-d) enlarged views of the copper segregations. (e) TEM EDX spectrum of the Cu segregation shown in (d) together with the (f) EELS spectrum acquired on the same segregation, compared with the spectrum of copper oxide and copper selected from Atlas library* [44].

TEM EDX analysis was performed to confirm that the smallest inclusions have the same nature as the large one. The TEM EDX spectrum, conducted on the ROI reported in Fig. 8d, is presented in Fig. 8e. Although both Cu Lα and Si Kα are clearly visible, the role of oxygen (O) in the composition of the segregations remains unclear. To gain further insights into this aspect, an EELS analysis was implemented. The corresponding EELS spectrum is shown as the red line in Fig. 8f. This spectrum was compared with a reference copper oxide EELS spectrum (blue line, Fig. 8f) from [38]. It becomes evident that the acquired spectrum lacks the edges at 948 eV (specific to Cu L2 in copper oxide, which is more intense than in metallic copper) and 532 eV (corresponding to the oxygen energy range). Consequently, we can deduce that the Cu inside the segregation has metallic-type bonds, and oxygen does not play a role in the chemical structure of the molecule.

The origin of the inclusion was found in a cross contamination that happened before the epitaxial growth. Probably the canister for wafer transportation was not properly cleaned. The following contamination in the contact areas was the route cause of the problems. In fact, Cu diffuses faster than Al, aurum (Au) and other metals in Si [45]. Variations in diffusion rates and mobility, process parameters, crystal defects and lattice strain can result in non-uniform distribution and the formation of differently sized segregations [46]. Metal impurities such as copper, iron, and nickel in silicon wafers have a detrimental impact on the performance and yield of semiconductor devices [47, 46, 48] in addition it can cause reliability risks of Si semiconductor devices [49, 50, 51].

## Conclusions

In this work, we presented a multiscale and multimodal correlative microscopy workflow for the comprehensive characterization of copper inclusions in the epitaxial layer of Superjunction Multi-drain MOSFETs. Copper inclusions can introduce defects in the crystal lattice, leading to localized areas of high resistance or conductivity and causing issues like high leakage (IDSS) or soft breakdown voltage (BVDSS). To address these challenges, we applied a combination of Light Microscopy (LM), X-ray Microscopy (XRM), Focused-Ion Beam Scanning Electron Microscopy (FIB-SEM) tomography, Energy Dispersive X-ray Spectroscopy (EDX), Transmission Electron Microscopy (TEM), and Electron Energy Loss Spectroscopy (EELS). The multimodal approach allowed us to gain insights into the morphology, topology, and chemistry of the copper inclusions across different length scales. Our findings revealed the distribution and characteristics of copper segregations with different shapes and sizes, providing a comprehensive understanding of their impact on the structural level of the power MOSFETs. This approach, which can be adopted in further workflows in the field of electronics and semiconductor failure analysis and research, is instrumental in addressing and mitigating issues related to epitaxial layers in Superjunction Multi-drain MOSFETs, offering valuable insights for improving device performance and reliability in power electronics applications.

## Acknowledgments

This work has been partially funded by ATOM project (Advanced TOmography and Microscopies) granted by Regione Lazio with the call “Open Infrastructure for research” (G11949, 04.09.2017) 2017.

## References


[1] C. Parisi, G. Belverde and A. Corsaro, "STMicroelectronics Super-Junction and UltraFAST MOSFET vs IGBT Technologies in Low Power Motor Drives," in *International Exhibition and Conference for Power Electronics, Intelligent Motion, Renewable Energy and Energy Management (PCIM Europe 2017)*, Nuremberg, 2017.

[2] C. Parisi and C. Mistretta, "The newest ST's Super-Junction Power MOSFET Technology for the Best Efficiency in Air Conditioning System," in *PCIM Europe 2018; International Exhibition and Conference for Power Electronics, Intelligent Motion, Renewable Energy and Energy Management*, Nuremberg, 2018.

[3] STMicroelectronics, "MDmesh," STMicroelectronics, 2023. [Online]. Available: https://www.st.com/en/power-transistors/mdmesh-m6-series.html.

[4] Carl Zeiss Microscopy, "Correlative Microscopy in Materials Science," 2017. [Online]. Available: https://www.zeiss.co.jp/content/dam/Microscopy/Products/Correlative%20Microscopy/book-correlative-microscopy-mat-science.pdf.

[5] T. Ando, S. P. Bhamidimarri, N. Brending, H. Colin-York, L. Collinson, N. De Jonge, P. J. de Pablo, E. Debroye, C. Eggeling and C. Franck, "The 2018 correlative microscopy techniques roadmap," *Journal of Physics D: Applied Physics*, vol. 51, 2018.

[6] T. L. Burnett, S. A. McDonald, A. Gholinia, R. Geurts, M. Janus, T. Slater, S. J. Haigh, C. Ornek, F. Almuaili, D. L. Engelberg, G. E. Thompson and P. J. Wither, "Correlative Microscopy," *Scientific Reports*, vol. 4, no. 4711, 2014.

[7] C. L. Fonta and B. M. Humbel, "Correlative microscopy," *Archives of Biochemistry and Biophysics*, vol. 581, pp. 98-110, 2015.

[8] S. K. Makineni, M. Lenz, P. Kontis, Z. Li, A. Kumar, F. J, S. Neumeier, M. Herbig, E. Spiecker, D. Raabe and B. Gault, "Correlative Microscopy—Novel Methods and Their Applications to Explore 3D Chemistry and Structure of Nanoscale Lattice Defects: A Case Study in Superalloys," *The Journal of The Minerals, Metals & Materials Society (TMS)*, vol. 70, pp. 1736-1743, 2018.

[9] R. L. Mitchell, P. Davies, P. Kenrick, T. Volkenandt, C. Pleydell-Pearce and R. Johnston, "Correlative Microscopy: a tool for understanding soil weathering in modern analogues of early terrestrial biospheres," *Scientific Reports*, vol. 11, 2021.

[10] Y. Leng, "Light Microscopy," in *Materials Characterization: Introduction to Microscopic and Spectroscopic Methods*, John Wiley & Sons (Asia) Pte Ltd, 2008, pp. 1-44.

[11] F. Cognigni, M. Pasquali, P. P. Prosini, C. Paoletti, A. Aurora, F. A. Scaramuzzo and M. Rossi, "X-Ray Microscopy: A Non-Destructive Multi-Scale Imaging to Study the Inner Workings of Batteries," *ChemElectroChem*, vol. 10, no. 7, 2023.

[12] D. Dini, F. Cognigni, D. Passeri, A. F. Scaramuzzo, M. Pasquali and M. Rossi, "Review—Multiscale Characterization of Li-Ion Batteries through the Combined Use of Atomic Force Microscopy and X-ray Microscopy and Considerations for a Correlative Analysis of the Reviewed Data," *Journal of The Electrochemical Society*, vol. 168, no. 12, 2021.

[13] H. Villarraga-Gómez, D. L. Begun, P. Bhattad, K. Mo, M. N. Rad, R. T. White and S. T. Kelly, "Assessing rechargeable batteries with 3D X-ray microscopy, computed tomography, and nanotomography," *Nondestructive Testing and Evaluation* , vol. 37, no. 5, 2022.

[14] S.-H. Yu, X. Huang, K. Schwarz, R. Huang, T. A. Arias, J. D. Brock and H. D. Abruña, "Direct visualization of sulfur cathodes: new insights into Li–S batteries via operando X-ray based methods," *Energy & Environmental Science*, vol. 11, pp. 202-210, 2018.

[15] C. Hartfield, C. Schmidt, A. Gu and S. T. Kelly, "From PCB to BEOL: 3D X-Ray Microscopy for Advanced Semiconductor Packaging," in *IEEE International Symposium on the Physical and Failure Analysis of Integrated Circuits (IPFA)*, Singapore, 2018.

[16] M. Oppermann, H. Roth, T. Neubrand and T. Zerna, "What's inside my USB drive? — X-ray microscopy and X-ray nano CT for 3D packaging," in *IEEE 15th Electronics Packaging Technology Conference (EPTC 2013)*, Singapore, 2013.

[17] Y. Zhao and J. Guo, "Development of flexible Li-ion batteries for flexible electronics," *InfoMat*, 2020.

[18] A. du Plessis and P. Rossouw, "X-ray computed tomography of a titanium aerospace investment casting," *Case Studies in Nondestructive Testing and Evaluation*, vol. 3, pp. 21-26, 2015.

[19] P. Chowdhury, H. Sehitoglu and R. Rateick, "Damage tolerance of carbon-carbon composites in aerospace application," *Carbon*, vol. 126, pp. 382-393, 2018.

[20] V. Giammaria, S. Boria, F. Sarasini, J. Tirillò, F. Cognigni, M. Rossi, B. Fischer and J. Pörnbacher, "Low-velocity impact behaviour of biocomposite laminates reinforced by flax, basalt and hybrid fibres at various temperatures: Analytical, numerical and experimental results," *Composite Structures*, vol. 322, 2023.

[21] J. Zhang, G. Liu, P. An, K. Yu, J. Huang, Y. Gu, J. Yao, R. Cao, H. Liu, C. Chen, C. Zhang and M. Wang, "The effect of cooling rates on crystallization and low-velocity impact behaviour of carbon fibre reinforced poly(aryl ether ketone) composites," *Composites Part B: Engineering*, vol. 254, 2023.

[22] M. Bernabale, F. Cognigni, C. Mancini, A. Proietti, F. Mura, D. Montanari, L. Nigro, M. Rossi and C. De Vito, "3D fractures analysis and conservation assessment of wrought iron javelin through advanced non-invasive techniques," *Scientific Reports*, vol. 13, 2023.

[23] M. Bernabale, F. Cognigni, F. Mura, L. Nigro, D. Montanari, M. Rossi and C. De Vito, "3D imaging of micro-segregation and corrosion behavior of alloying elements in archaelogical artefacts from Motya (Sicily, Italy)," *Corrosion Science*, vol. 211, 2023.

[24] M. Bernabale, F. Cognigni, L. Nigro, M. Rossi, T. De Caro and C. De Vito, "A comprehensive strategy for exploring corrosion in iron-based artefacts through advanced Multiscale X-ray Microscopy," *Scientific Reports*, vol. 12, no. 1, 2022.

[25] M. Bernabale, F. Cognigni, L. Nigro, M. Rossi and C. De Vito, "Conventional and advanced techniques for archaelogical diagnostic of iron artefacts," in *2022 IMEKO TC-4 International COnference on Metrology for Archaeology and Cultural Heritage University of Calabria*, Cosenza, 2022.

[26] S. Mamidwar, M. Weiner, H. Alexander and J. Ricci, "In Vivo Bone Response to Calcium Sulfate/Poly l-Lactic Acid Composite," *Implant Dentistry*, vol. 17, no. 2, pp. 208-216, 2008.

[27] Y.-F. Wang, C.-Y. Wang, P. Wan, S.-G. Wang and X.-M. Wang, "Comparison of bone regeneration in alveolar bone of dogs on mineralized collagen grafts with two composition ratios of nano-hydroxyapatite and collagen," *Regenerative Biomaterials*, vol. 3, no. 1, pp. 33-40, 2016.

[28] F. Cognigni, S. Dinarelli, M. Girasole, G. Longo, G. Fabi and M. Rossi, "3D X-ray Microscopy (XRM) investigation of exogenous materials inside mussels' organs," in *NanoInnovation 2021*, 2022.

[29] A. P. Merkle and J. Gelb, "The Ascent of 3D X-ray Microscopy in the Laboratory," *Microscopy Today*, vol. 21, no. 2, pp. 10-15, 2013.

[30] U. Stachewicz, P. K. Szewczyk, A. Kruk, A. H. Barber and A. Czyrska-Filemonowicz, "Pore shape and size dependence on cell growth into electrospun fiber scaffolds for tissue engineering: 2D and 3D analyses using SEM and FIB-SEM tomography," *Materials Science and Engineering: C*, vol. 95, pp. 397-408, 2019.

[31] K. Kulawik, P. A. Buffat, A. Kruk, A. M. Wusatowska-Sarnek and A. Czyrska-Filemonowicz, "Imaging and characterization of γ′ and γ″ nanoparticles in Inconel 718 by EDX elemental mapping and FIB–SEM tomography," *Materials Characterization*, vol. 100, pp. 74-80, 2015.

[32] C. S. S. R. Kumar, Transmission Electron Microscopy Characterization of Nanomaterials, Springer Berlin, Heidelberg, 2014.

[33] R. F. Egerton, "Electron energy-loss spectroscopy in the TEM," *Reports on Progress in Physics*, vol. 72, 2009.

[34] Carl Zeiss - Research Microscopy Solutions, "ZEISS ZEN core - Software Suite for Connected Microscopy from the Materials Lab to Production," Carl Zeiss - Research Microscopy Solutions, 2023. [Online]. Available: https://www.zeiss.com/microscopy/en/products/software/zeiss-zen-core.html.

[35] Carl Zeiss - Research Microscopy Solutions, "ZEISS ZEN Connect - Visualize Image and Data in Context," Carl Zeiss - Research Microscopy Solutions, 2023. [Online]. Available: https://www.zeiss.com/microscopy/en/resources/insights-hub/manufacturing-assembly/visualize-images-and-data-in-context---zeiss-zen-connect.html.

[36] Synopsys, "Yield Management - Avalon - CAD Navigation and Debug Solutions for Failure Analysis," Synopsys, 2023. [Online]. Available: https://www.synopsys.com/silicon/yield-management/avalon.html.

[37] Carl Zeiss - Research Microscopy Solutions, "ZEISS Atlas 5 - Master Your Multi-scale Challange," Carl Zeiss - Research Microscopy Solutions, 2023. [Online]. Available: https://www.zeiss.com/microscopy/en/products/software/zeiss-atlas-5.html.

[38] Carl Zeiss - Research Microscopy Solutions, "Scout-and-Scan Instrument Control System," Carl Zeiss - Research Microscopy Solutions, 2023. [Online]. Available: https://www.zeiss.com/microscopy/us/l/campaigns/scout-and-scan.html.

[39] L. A. Feldkamp, L. C. Davis and J. W. Kress, "Practical cone-beam algorithm," *Journal of the Optical Society of America A*, vol. 1, no. 6, pp. 612-619, 1984.

[40] Object Research Systems (ORS) Inc., "Dragonfly is the Premier Software Platform for Scientific Image Processing," Object Research Systems (ORS) Inc., 2023. [Online]. Available: https://theobjects.com/index.html.

[41] Z. Zhang, W. Wang, Z. Dong, X. Yang, F. Liang, X. Chen, C. Wang, C. Luo, J. Zhang, X. Wu, L. Sun and J. Chu, "The Trends of In Situ Focused Ion Beam Technology: Toward Preparing Transmission Electron Microscopy Lamella and Devices at the Atomic Scale," *Advanced Electronic Materials*, vol. 8, no. 9, 2022.

[42] Carl Zeiss - Research Microscopy Solutions, "ZEISS Xradia Versa X-ray Microscopes," 2023. [Online]. Available: https://www.zeiss.com/microscopy/en/products/x-ray-microscopy/xradia-versa.html.

[43] W. H. Walton, "Feret‘s Statistical Diameter as a Measure of Particle Size," *Nature*, vol. 162, pp. 329-330, 1948.

[44] Gatan Corporate, "EELS Atlas," Gatan Corporate, 2023. [Online]. Available: https://eels.info/atlas.

[45] W. Frank, "Diffusion in Crystalline Silicon and Germanium — the State-of-the-Art in Brief," in *Crucial Issues in Semiconductor Materials and Processing Technologies*, 1992, pp. 383-402.

[46] K. Graff, Metal Impurities in Silicon-Device Fabrication, Springer Berlin, Heidelberg, 2000.

[47] R. Ozaki, K. Torigoe, T. Mizuno and K. Yamamoto, "Gettering Mechanism of Copper in n-Type Silicon Wafers," *physica status solidi*, vol. 216, no. 17, 2019.

[48] H. A. Bakar, Z. Awang and W. A. A. W. Razali, "Determination of copper contamination from various sources in an RFIC wafer fab using VPD -TXRF methodology," in *Asia-Pacific Conference on Applied Electromagnetics, APACE*, Melaka, 2007.

[49] A. A. Istratov, C. Flink, H. Hieslmair, S. A. McHugo and E. R. Weber, "Diffusion, solubility and gettering of copper in silicon," *Materials Science and Engineering: B*, vol. 72, no. 2-3, pp. 99-104, 2000.

[50] A. A. Istratov and E. R. Weber, "Physics of Copper in Silicon," *Journal of The Electrochemical Society*, vol. 149, 2001.

[51] R. Mehta, S. Chugha and Z. Chen, "Transfer-free multi-layer graphene as a diffusion barrier," *Nanoscale*, vol. 9, no. 5, pp. 1827-1833, 2017.